Journal of Materials Chemistry A

Accepted Manuscript

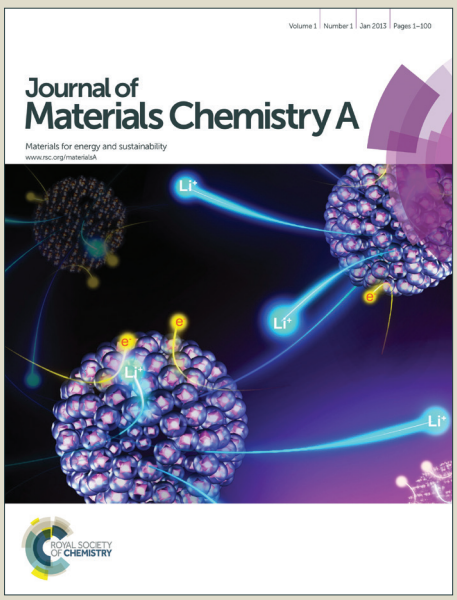

ROYAL SOCIETY OF CHEMISTRY

www.rsc.org/materialsA

Soft chemical *in-site* synthesis, formation mechanism and electrochemical performances of 1D bead-like $AgVO_3$ nanoarchitectures

Xingang Kong[a], Zhanglin Guo[a], Chaobin Zeng[a], Jianfeng Huang[a]*, Liyun Cao[a], Li Li[a], Lixiong Yin[a], Puhong Wen[b], Qi Feng[c], Zhanwei Xu[a]*

[a] School of Materials Science and Engineering, Shaanxi University of Science and Technology, Weiyang, Xi'an, Shaanxi 710021, PR China

[b] Department of Chemistry and Chemical Engineering, Baoji University of Arts and Science, 1 Gaoxin Road, Baoji, Shaanxi 721013, PR China

[c] Department of Advanced Materials Science, Faculty of Engineering, Kagawa University, 2217-20 Hayashi-cho, Takamatsu-shi, 761-0396 Japan

*Author to whom correspondence should be addressed. E-mail: huangjf@sust.edu.cn, davidemt@126.com

Abstract

The soft chemical process is a useful and unique method for preparation and design of one-dimensional (1D) nanoarchitectures. The 1D bead-like $AgVO_3$ nanoarchitectures are prepared via the soft chemical *in-site* reaction using the layered structure $K_2V_6O_{16}\cdot 2.7H_2O$ platelike particles as precursor. The formation mechanism is investigated through tracing the evolution of structure and morphology of intermediate products during the reaction, and it contains two processes. One is the *in site* reaction of the Ag^+ ions with the V_3O_8 layers of $K_2V_6O_{16}$. The other is the fragmentation of the 2D platelike composite into 1D fiber composite. Moreover, the electrochemical investigation shows that after 50 cycles at the current density of 100 $mA\cdot g^{-1}$, the 1D bead-like nanostructures cathode exhibits a higher discharge capacity (127 $mAh\cdot g^{-1}$) than that of 1D nanowires (75 $mAh\cdot g^{-1}$), mainly due to the larger specific surface area and fine particles constructed architectures.

Introduction

The soft chemical process is a useful and unique method for preparation and design of function inorganic materials.[1–3] This process typically comprises two steps: the first step is the preparation of a framework precursor with layered or tunnel structure and insertion of template ions or molecules into the interlayer space by ion-exchange reaction, and the second step is the transformation of the template-inserted precursor into a desired structure under the moderate condition, such as the solvotherrmal, hydrothermal treatment, or the low temperature heat-treatment. The crystal structure of the product can be controlled by the used template, and the product particle morphology is dependent on the morphology of the used precursor. This method has been utilized for the synthesis and design of metal oxides nanomaterials with controlled structure, morphology, and chemical composition.[4–6]

In previous study of controlling chemical composition, structure, morphology, and grain size of

particle, we have synthesized some two-dimensional (2D) and one-dimensional (1D) particles, for example, $Ba_{0.5}(Bi_{0.5}K_{0.5})_{0.5}TiO_3$,[7] $Ba_{0.9}Ca_{0.1}TiO_3$,[8] $AgNbO_3$,[9] $ZnNb_2O_6/KNbO_3$,[10] $LiNbO_3/KNbO_3$[11]. The preparation of all of these particles use the open structure compound with layered or tunnel framework as precursor through the soft chemical process, in which the Ba^{2+}, Zn^{2+} or Ag^{+} ions et al. easily intercalate into the interlayer or tunnel of precursor, and *in site* react with the framework of precursor to form the target particles. It is characteristic that all of these target particles are nanoarchitectures, which are constructed from nanoparticles.

Nanostructures have attracted considerable attention due to their distinct electronic, optical, photocatalytic, magnetic properties, and so on, which differ from their bulk counterparts. For example, nanostructures used as energy storage materials exhibit good electrochemical properties because of their shortened diffusion paths and increased contact areas between the electrolyte and the electrode for Li^{+} insertion/extraction.[12-14] Recently, silver vanadium oxides ($AgVO_3$,[15-17] $Ag_2V_4O_{11}$,[18] $Ag_4V_2O_6F_2$,[19] and $Ag_{0.33}V_2O_5$[20]) as cathode materials in lithium-ion batteries and photocatalyst for organic pollution degradation have been well investigated and have been employed as cathode materials in commercial primary lithium batteries for many years. Especially, β-$AgVO_3$ is suited for application in implantable medical devices,[21, 22] due to its higher Ag/V molar ratio, higher discharge capacity, and long-term chemical and structural stability.[15] It is generally accepted that the smaller the particles is, meaning higher specific surface area and closer interfaces of particles, the smaller the electron transport resistance and the shorter diffusion paths are, which benefit for improving the storage capacity and the electrical conductivity of β-$AgVO_3$ as cathode materials.[23] Therefore, a large number of nanostructural β-$AgVO_3$ materials have been fabricated, for example nanorods,[23] nanowires,[24, 25] nanoribbons,[26] nanoneedles,[27] nanobelts,[28] all of which are the 1D single nanocrystals. It is well known that the

equiaxial nanoparticles possess a larger specific surface area comparing with the 1D single nanocrystals, but often suffer from the self-aggregation in their applications, which may reduce the effective contact areas of active materials with conductive additives and electrolytes.[29] Thus, if the assembling 1D β-$AgVO_3$ nanoarchitectures with equiaxial nanoparticles are formed, the self-aggregation can be effectively prevented and the larger effective contact areas can be ensured, so that the storage capacity of β-$AgVO_3$ cathode materials will be improved further. However, there are few papers reported the synthesis and electrochemical properties of the 1D $AgVO_3$ nanoarchitectures so far.

At present, the $AgVO_3$ nanomaterials are mainly prepared via using V_2O_5, NH_4VO_3 or V foils as Vanadium sources and $AgNO_3$ or Ag_2O as Silver source under the hydrothermal, microwave-assisted hydrothermal or room-temperature condition.[30-33] And the formation of these $AgVO_3$ nanostructures almost follows the dissolution-crystallization mechanism, in which $AgVO_3$ grow along 1D direction orientation according to its growth habits, resulting in the 1D single nanocrystals,[33] but not the nanoarchitectures constructed from nanoparticles. Therefore, it is a challenge to build 1D $AgVO_3$ nanoarchitectures.

In this paper, we report the preparation of 1D bead-like $AgVO_3$ nanoarchitectures by using the layered $K_2V_6O_{16}\cdot 2.7H_2O$ platelike particle as precursors under the room-temperature condition. The formation reaction mechanism and the electrochemical properties of the 1D $AgVO_3$ nanostructures are investigated. Such a bead-like 1D $AgVO_3$ nanoarchitectures is very difficult to prepare via the normal method, because of its growth habits along 1D orientation. The success in preparing the bead-like 1D $AgVO_3$ nanoarchitectures constructed from nanoparticles is significant for electrode materials of high-performance Li ion batteries.

Experimental Section

Preparation of layered $K_2V_6O_{16}\cdot 2.7H_2O$ precursor

The preparation of 2D platelike $K_2V_6O_{16}\cdot 2.7H_2O$ precursor has been reported in our previous literature.[34] In a typical process, 0.5 g of V_2O_5 and 40 mL of 0.3 $mol\cdot L^{-1}$ KOH water solution were placed in a Teflon -lined, sealed stainless-steel vessel with an inner volume of 100 mL and stirred to form clear solution. Then the pH value of the solution was adjusted to around 6 with 2 $mol\cdot L^{-1}$ HCl solution under the magnetic stirring, afterwards hydrothermally treated at 180 ^oC for 12 h under stirring condition. After the hydrothermal treatment, a precipitation was obtained, and then the sample was filtered, washed with distilled water and dried at room temperature.

Preparation of 1D α-$AgVO_3$ and β-$AgVO_3$ nanoarchitectures

0.5 g of $K_2V_6O_{16}\cdot 2.7H_2O$ samples were put into 100 mL of 0.5 $mol\cdot L^{-1}$ $AgNO_3$ aqueous solution, then magnetic stirred in order to reaction proceeded for 24 h at room temperature and the pH values of the solution were recorded. After reaction, the products were filtered, washed with distilled water, and dried at room temperature. Finally, the as-prepared samples were heat-treated at 200 ^oC and 300 ^oC for 2 h to obtain pure phase β-$AgVO_3$. The obtained samples were denoted as β-200 and β-300, respectively.

Preparation of β-$AgVO_3$ nanowires

β-$AgVO_3$ nanowires (β-NWs) were selected as a comparison and synthesized via the process reported in the literature.[35] An amount of 0.1359 g of $AgNO_3$ (0.8mmol) was dissolved into 8 mL of deionized water, and equal molar NH_4VO_3 was dissolved into another 8 mL of deionized water at 80°C. After that, the NH_4VO_3 solution was added slowly to the $AgNO_3$ solution under stirring. An orange precipitate formed immediately. After the mixture had been stirred for about 10 min, the resulting

precursor suspension was transferred into a 25 mL Teflon-lined stainless steel autoclave. The autoclave was sealed and heated at 180°C for 12 h. After the reaction, the autoclave was cooled to ambient temperature naturally. The final products were collected by centrifugation, washed with deionized water and ethanol, and then vacuum dried at 60°C for 4 h.

Physics analysis

The crystal structure of the sample was investigated using a powder X-ray diffractometer (XRD, Rigaku D/max-2200PC) with Cu Kα (λ=0.15418 nm) radiation. The size and morphology of the particles were observed using field-emission scanning electron microscopy (Hitachi, FE-SEM, S-4800). Transmission electron microscopy (TEM,) observation and selected-area electron diffraction (SAED) were performed on a Tecnai G^2F20S-TWIN system at 200 kV, and the powder sample was supported on a micro grid. Thermo Gravimetric and Differential Scanning Calorimetry (TG-DSC) were conducted on a DTG-60H thermo gravimetric analyzer (Shimadzu). X-ray photoelectron spectroscopy (XPS) measurements were done on an Axis Ultra XPS instrument with an Mg Kα source. The Raman spectrum measurements of the samples were operated on the Renishaw-invia with a laser at 532 nm. Specific surface areas were calculated based on the Brunauer–Emmett–Teller (BET) method.

Electrochemical measurements were performed using CR2032 coin-type cells assembled in an argon-filled glove box. To prepare cathode materials as working electrode, the synthesized β-$AgVO_3$, polyvinylidene fluoride (PVDF) binder and acetylene black were mixed together at a weight ratio of 70:20:10 in N-methylpyrrolidinone (NMP). The electrolyte consisted of a solution of 1 M LiPF6 in ethylene carbonate and dimethyl carbonate (EC+DMC, 1:1 in volume). The electrochemical performances of the samples were examined with lithium as counter electrode. The cells were cycled between 1.5 and 4.0 V at various current densities with a multichannel battery testing system

(Shenzhen, Neware, China). Cyclic voltammograms (CV), recorded at scan rates of 0.1 mV/s, and electrochemical impedance spectroscopy (EIS) analysis were performed using CHI660E electrochemical station (Shanghai Chenhua, China).

Result and discussion

Structure and morphology

We have previously reported the hydrothermal synthesis of the layered $K_2V_6O_{16}\cdot 2.7H_2O$ platelike particles with fine crystallinity (Fig.1a), which consist of V_3O_8 layers and interlaminar hydrated K^+ ions. In the synthesis process of silver vanadates, this layered $K_2V_6O_{16}\cdot 2.7H_2O$ platelike particle is used as precursor and treated in the $AgNO_3$ aqueous solution via the magnetic stirring at room temperature. Usually, the interlaminar alkali metal ions of layered or tunnel structure compound can be exchanged by other ions, and their layered or tunnel framework structure is retained, such as $K_{0.8}Ti_{1.73}Li_{0.27}O_4$[36], $K_4Nb_6O_{17}$[37], $K_2Ti_4O_9$[38]. After the treatment of $K_2V_6O_{16}\cdot 2.7H_2O$ precursor in the $AgNO_3$ solution for 24 h, however, the product has not kept the layered structure of precursor, and displays a pure α-$AgVO_3$ phase (JCPDS No. 89-4396) with fine crystalline (Fig. 1b). It is indicated that it is not a simple exchange reaction of the Ag^+ ion with the interlaminar K^+ ions of $K_2V_6O_{16}\cdot 2.7H_2O$ phase during the treatment of $K_2V_6O_{16}\cdot 2.7H_2O$ precursor in the $AgNO_3$ solution.

It is well known that α-$AgVO_3$ phase occurs to phase transition at about 200 °C, and changes into β-$AgVO_3$ phase.[31] The TG-DTA curves of as-obtained α-$AgVO_3$ product by us shows that there is an exothermic peak of phase transition at 185 °C (Fig S1), which is similar to literature.[33] So we heat-treat α-$AgVO_3$ product at 200 ^oC and 300 ^oC for 2h, respectively. XRD patterns of heat-treated samples are shown in Fig 1c and 1d. It is found that the sample obtained at 200 ^oC mainly displays the β-$AgVO_3$ phase (JCPDS No. 86-1154), except the residual α-$AgVO_3$ phase (a weak peak at $2\theta=32.18^o$ in Fig. 1c).

When the heat-treatment temperature increases to 300 ^{o}C, the α-$AgVO_3$ phase has completely transformed into the pure β-$AgVO_3$ phase (JCPDS No. 86-1154), and the crystallinity of β-$AgVO_3$ phase enhances.

FE-SEM image shows that the obtained α-$AgVO_3$ sample displays a 1D fiberlike shape, where the fibers are about 50 nm in width and 5μm in length (Fig. 2b). These fibers are consisted of the α-$AgVO_3$ nanocrystals (size of about 5nm) via beading, meanings the 1D bead-like α-$AgVO_3$ nanoarchitectures. After the 1D bead-like α-$AgVO_3$ nanoarchitectures being respectively heat-treated under 200 ^{o}C and 300 ^{o}C, the obtained β-$AgVO_3$ samples, which are respectively noted as β-200 and β-300, both present the 1D bead-like morphology (Fig. 2c and d). There is a difference that the particle size of β-300 (about 10nm) is slightly larger than that of β-200 (about 5nm).

Similar to the FE-SEM results, the TEM images also show that both the α-$AgVO_3$ and β-300 sample have 1D filamentous shapes (Fig. 3a and c) and are constructed from nanocrystals. In HRTEM image of the 1D bead-like α-$AgVO_3$ nanoarchitectures (Fig. 3b), we observe the lattice fringes of the α-$AgVO_3$ phase with the lattice spacing of $d_{(002)}$ = 0.368 nm and $d_{(110)}$ =0.286 nm, and the additional lattice spacing of a single nanoparticles is 0.238 nm, which can be indexed to the (111) spacing of the Ag phase (JCPDS No. 03-0921). Similarly, the HRTEM image of the 1D bead-like β-300 nanoarchitectures also reveals the existence of the Ag phase (JCPDS No. 03-0921, $d_{(111)}$ = 0.238 nm), except the lattice fringes of the β-$AgVO_3$ phase with the lattice spacing of $d_{(002)}$ = 0.368 nm and $d_{(110)}$ =0.286 nm. These Ag nanoparticles may appear because of the decomposition of $AgVO_3$ nanoparticles as a result of high-energy electron irradiating during the HRTEM observation. The above results demonstrate that the 1D bead-like $AgVO_3$ nanoarchitectures can be easily synthesized via using the platelike $K_2V_6O_{16}\cdot 2.7H_2O$ particle as precursor.

To further confirm whether the Ag nanoparticles generate during our synthesis of 1D bead-like $AgVO_3$ nanoarchitectures, XPS was employed to investigate the silver valence state and composition of the samples. Figure 4a shows the overall XPS spectrum of the 1D α-$AgVO_3$ nanoarchitectures. The binding energies obtained in the XPS analysis were calibrated for specimen charging by referencing the C 1s to 284.6 eV. It is found that no peaks of other elements except C, O, Ag, and V were observed in the survey spectrum (Fig. 4a), indicating that no $K_2V_6O_{16}\cdot 2.7H_2O$ phase exists in the nanoarchitectures product. The Ag 3d XPS spectrum only displays two peaks at 367.3 and 373.3 eV (Fig. 4b), assigning to Ag $3d^{5/2}$ and Ag $3d^{3/2}$ of Ag^+, indicating the valence state of all silver element is +1 in the 1D nanoarchitectures[16-19, 26, 35, 39]. The two peaks located at 516.6 and 524.1 eV are corresponded to V $2p^{3/2}$ and V $2p^{1/2}$ of V^{5+}, respectively[16-19, 26, 35, 40](Fig. 4c). The obtained atomic ratio of the Ag/V in $AgVO_3$ is 1:1.09, which is almost the same to the stoichiometric composition of α-$AgVO_3$. Therefore, it can be affirmed that no Ag nanoparticles generate during our synthesis of 1D bead-like α-$AgVO_3$ nanoarchitectures. In addition, the 1D bead-like β-300 nanoarchitectures also presents the same XPS spectrum to the 1D α-$AgVO_3$ nanoarchitectures (Fig. S2), revealing that no Ag nanopaticles generate during the heat-treatment of 1D α-$AgVO_3$ nanoarchitectures.

Fig. 5a shows the Raman spectrum of 1D bead-like α-$AgVO_3$ nanoarchitectures, which agrees with that of 1D *α*-$AgVO_3$ nanowires reported by Singh *et al*.[41] The strongest band at 920 cm^{-1} may originate from either bridging V-O-Ag or O-V-O vibrations. The band at 892 cm^{-1} can be associated with the stretching vibrations of VO_3 groups in the $(V_2O_7)^{4-}$ cluster ion. The band at 815 cm^{-1} can be assigned to stretching vibrations of the Ag-O-Ag bridges. The bridging V-O-V bond in the polymeric metavanadate chains are reflected by the 740, 630 and 527 cm^{-1} bands, corresponding to the asymmetric and symmetric stretches, respectively. And others peaks located at 498, 309, 215, and 167

cm^{-1} may belong to the α-$AgVO_3$ phase.[41]

Fig. 5b, c and d respectively show the Raman spectra of β-200, β-300 and the β-$AgVO_3$ (β-NWs) sample obtained by the literature's method (Fig. S3). It is found that all β-$AgVO_3$ samples display almost the same band positions. The strongest band at 887 cm^{-1} may originate from either bridging V-O-Ag or O-V-O vibrations. The band at 845 cm^{-1} can be associated with the stretching vibrations of VO_3 groups in the $(V_2O_7)_4$ ion. The band at 808 cm^{-1} can be assigned to stretching vibrations of the Ag-O-Ag bridges. The bridging V-O-V bond in the polymeric metavanadate chains is reflected by the 732 and 517 cm^{-1} bands, corresponding to the asymmetric and symmetric stretches, respectively. These peaks along with those located at 390, 340, 249, and 172 cm^{-1} are the clear signatures of the $AgVO_3$, which are the same with those of the results reported by literatures.[22, 24, 26, 42] However, in Fig. 5b, the spectrum of the β-200 sample, there is a weak absorption band at 920 cm^{-1}, which should be ascribed to the bridging V-O-Ag or O-V-O vibrations of α-$AgVO_3$ phase. This is consistent with the XRD result (Fig. 1c).

Although the band positions of all prepared β-$AgVO_3$ samples are the same in Raman spectra, there are differences in the relative peak intensities of absorption band. The intensity ratios of peaks at 887 cm^{-1} (the first order peak) to 808 cm^{-1} (the second order peak) of β-200, β-300 and β-NWs are 1.94, 1.86 and 1.18, respectively. The peaks intensity ratio of Raman spectrum is correlated with the particle size of nanomaterials.[43] As for nanomaterials, decreasing the grain size leads to an increase in quantum confinement, which leads an increase in the optical bandgap of the material. This increase is reflected in varied photoluminescence emissions from the free exciton energy, and preferentially enhances the main Raman peak, or the second order peak.[43-45] It is implied that the three samples should possess the different particle size and specific surface areas. BET results (Fig. S4) show that β-200, β-300 and

β-NWs samples have the surface area of 94, 83, and 24 $m^2 g^{-1}$, respectively.

Evolution of structure and morphology

To study the formation mechanism and morphology evolution from 2D platelike $K_2V_6O_{16}·2.7H_2O$ particle to 1D bead-like α-$AgVO_3$ nanoarchitectures, we operate the different reaction time at room temperature. Fig. 6 presents the XRD patterns of samples obtained via the treatment of the platelike $K_2V_6O_{16}·2.7H_2O$ in the $AgNO_3$ solution at room temperature for different times. After the treatment for 1h, all diffraction peaks of the obtained sample are consistent with that of the $K_2V_6O_{16}·2.7H_2O$ precursor, and the characteristic peak of the layered structure at around $2\theta=10^o$ has no shift, suggesting that there are no Ag^+ ions in the interlayer of $K_2V_6O_{16}·2.7H_2O$ phase. When the treatment time is 4h, the diffraction peaks of the α-$AgVO_3$ phase are clearly observed except that of the unreacted $K_2V_6O_{16}·2.7H_2O$ phase. The diffraction peaks of $K_2V_6O_{16}·2.7H_2O$ phase gradually weaken as the reaction time is prolonged, meanwhile the diffraction peak intensity of the α-$AgVO_3$ phase increases. When the treatment time prolongs to 24 h, the layered structure $K_2V_6O_{16}·2.7H_2O$ phase have completely changed into the α-$AgVO_3$ phase. It is found that in the total transformation process from the pure $K_2V_6O_{16}·2.7H_2O$ phase to the pure α-$AgVO_3$ phase, the characteristic peak of the unreacted $K_2V_6O_{16}·2.7H_2O$ phase at around $2\theta=10^o$ all has no shift, indicating that the Ag+-exchanged $K_2V_6O_{16}·2.7H_2O$ phase with layered structure should be transient state, and it cannot exists steadily.

Moreover, the system pH value during the reaction was also continuously monitored and is shown in Tab. S1. The pH value of $AgNO_3$ solution (0.5 mol L^{-1}) is 5.70 before the reaction. The pH value of reaction system immediately decreases to 4.72 after the $K_2V_6O_{16}·2.7H_2O$ precursor is put into the $AgNO_3$ solution. With prolonging the reaction time, the pH value of the system gradually reduces,

up to 24 h, tend to be stable (pH=2.21). It is suggested that the H^+ ions are generated in the formation reaction of the α-$AgVO_3$ phase, and the chemical reaction equation could be described as:

$$\mathbf{K_2V_6O_{16}+6Ag^++2H_2O\rightarrow 6AgVO_3+4H^++2K^+} \quad \mathbf{(1)}$$

According to the rapid decrease of the system pH value after adding the $K_2V_6O_{16}\cdot 2.7H_2O$ precursor into the $AgNO_3$ solution, it can be concluded that the reaction of the Ag^+ ions with the $K_2V_6O_{16}\cdot 2.7H_2O$ precursor is very quick. Therefore, we deduce that the Ag^+ ions contact with the V_3O_8 layers of $K_2V_6O_{16}$ phase or intercalate the V_3O_8 interlayer via K^+/Ag^+ ion-exchange, and straightway react with V_3O_8 layers to *in site* generate the α-$AgVO_3$ phase, implying that the Ag^+ ions cannot steadily exist in the V_3O_8 interlayer of $K_2V_6O_{16}$ phase. Therefore, the diffraction peaks of Ag^+-exchanged $K_2V_6O_{16}$ phase cannot be observed in the XRD patterns.

Fig. 7 shows FE-SEM images of products obtained after the treatment for 1h, 4h, 8h and 12h, respectively. The treated $K_2V_6O_{16}\cdot 2.7H_2O$ sample for 1h still keep the platelike morphology. And some nanoparticles with the size of about 5 nm are clearly observed on the surface of the platelike particle. These nanoparticles could be attributed to the α-$AgVO_3$ phase formed via *in site* reaction, although the α-$AgVO_3$ phase cannot be detected in the XRD pattern due to the low content of nanoparticles.

After the treatment for 4h, the mixed phase sample of $K_2V_6O_{16}\cdot 2.7H_2O$ and α-$AgVO_3$ presents two different types of particles with platelike and fiberlike shapes (Fig. 7b). This platelike particle corresponds to the unreacted $K_2V_6O_{16}$ phase. This fiberlike particle is the size of about 500nm in width. FE-SEM and TEM all present that this fiber fill with nanoparticles with the size of 5nm on the surface (inserted Fig. 7b and Fig. 8a). It is interesting that the SAED pattern of this fiber displays a set of clear diffraction spot and the diffraction circles of polycrystal (inserted Fig. 8a). The diffraction spots with d-values of 0.49nm and 0.55 nm correspond to the (100) and (011) planes of the $K_2V_6O_{16}\cdot 2.7H_2O$

phase, whereas the d-values of diffraction circles are 0.21nm and 0.12 nm, which is attributed to the (222) and (224) planes of the α-$AgVO_3$ polycrystal. It is indicated that this fiber is 1D $K_2V_6O_{16}\cdot 2.7H_2O$ single crystal which is *in site* overgrown with α-$AgVO_3$ nanoparticles on the surface. Therefore, it is confirmed that this fiber is a 1D composite that consist of the $K_2V_6O_{16}\cdot 2.7H_2O$ single crystal and the α-$AgVO_3$ nanoparticles, meanings the $K_2V_6O_{16}$/α-$AgVO_3$ composite fiber. In addition, we find that during the TEM observation, the nanoparticles on the composite fiber will gradually increase under the irradiation of electron beam for 20 seconds, which has been clearly observed as shown in Fig. S5. The growth of these nanoparticles is due to the bombardment of high-energy electrons during the TEM observation.[26]

After the treatment for 8h, the platelike $K_2V_6O_{16}\cdot 2.7H_2O$ particles disappears from the obtained sample, and the thin fiber with the size of 50nm in width is discovered except the thick $K_2V_6O_{16}$/α-$AgVO_3$ composite fiber (Fig. 7c and 8b). When the treatment time is prolonged to 12h, the obtained sample only is composed of the thin fiber with the size of 50nm in width. This thin fiber is also bestrewed with nanoparticles with the size of 5nm on the surface (Fig. 7d and 8c). The SAED pattern of this thin 1D fiber shows the weak diffraction spot of the $K_2V_6O_{16}\cdot 2.7H_2O$ phase and the clear diffraction circles of the α-$AgVO_3$ phase. In addition, the lattice fringes of the $K_2V_6O_{16}\cdot 2.7H_2O$ phase can be found in HRTEM image of part of thin fiber, that are the lattice spacing of $d_{(002)}$ = 0.368 nm and $d_{(110)}$ =0.286 nm. It is indicated that the thin fiber is also a $K_2V_6O_{16}$/α-$AgVO_3$ composite, merely in which the α-$AgVO_3$ phase occupies the main portion, which is also consistent with the XRD results. Until the treatment for 24 h, the obtained α-$AgVO_3$ product with high purity is the 1D bead-like nanoarchitectures, which is constructed from nanocrystals via beading together (Fig. 2b).

In general, all samples obtained at different treatment time are overgrown with $AgVO_3$

nanocrystals on the surface, and the shape evolution of these samples is from 2D platelike to thick 1D fiberlike, and then to thin 1D fiberlike with the extension of treatment time. Moreover, the $AgVO_3$ nanocrystal sizes of these nanoarchitectures almost have no change, suggesting that the formation of the $AgVO_3$ nanocrystal is an *in site* crystallization but not the dissolution-crystallization.

Formation mechanism of the 1D bead-like α-$AgVO_3$ nanoarchitectures

On the basis of above results, we propose a formation mechanism of the 1D bead-like $AgVO_3$ nanoarchitectures from the 2D layered $K_2V_6O_{16}{\cdot}2.7H_2O$ platelike particle, as shown in Fig. 9. The formation reaction of the 1D bead-like α-$AgVO_3$ nanostructures contains mainly two processes of *in site* crystallization and fragmentation. Firstly, the Ag^+ ions contact with the V_3O_8 layers of $K_2V_6O_{16}{\cdot}2.7H_2O$ phase or intercalate the V_3O_8 interlayer via K^+/Ag^+ ion-exchange, and then straightway *in site* react with V_3O_8 layers to generate the α-$AgVO_3$ nanocrystal. These nanocrystal are inlaid into the substrate of the unreacted $K_2V_6O_{16}{\cdot}2.7H_2O$ phase. At the same time, the reaction releases the H^+ ions, which rapidly reduce the system pH value (Tab. S1). As the *in site* reaction progresses, the system pH value continually decreases and the fragmentation proceeds. The 2D layered $K_2V_6O_{16}$ platelike particle is not steady under the condition of pH=2~4, and easily split into the 1D layered $K_2V_6O_{16}$ fiber, which had been described by our previous paper in detail.[34] In addition, *in site* formation of $AgVO_3$ phase within $K_2V_6O_{16}$ phase leads to the destruction of the local layered structure within $K_2V_6O_{16}$ phase. Therefore, the 2D $K_2V_6O_{16}$/α-$AgVO_3$ composite plate is easier to divide into the thick $K_2V_6O_{16}$/α-$AgVO_3$ composite fiber (Fig. 7b and 8a) as the Ag^+ ions constantly *in site* react with the unreacted $K_2V_6O_{16}$ phase within the composite. With further destruction of the layered structure, these thick composite fibers continue to divides into the thin $K_2V_6O_{16}$/α-$AgVO_3$ composite fibers (Fig. 7d and 8c). Finally, when the unreacted $K_2V_6O_{16}$ phase within the thin composite fiber is thoroughly

depleted, the thin fiber no longer split, but transforms into a 1D bead-like α-$AgVO_3$ nanoarchitectures. The α-$AgVO_3$ is a metastable phase and it can be irreversibly transformed into the stable β-$AgVO_3$ phase during the heat-treatment.

The mechanism described above suggests that the layered open structure of $K_2V_6O_{16}$ precursor is important to form the 1D bead-like nanoarchitectures in the formation process of the $AgVO_3$ phase.

Electrochemical Properties

Fig. 10a displays the electrochemical performance of the bead-like β-300 nanoarchitectures samples compared to the β-$AgVO_3$ nanowires sample cathodes tested at the current density of 100 $mA \cdot g^{-1}$. The initial capacity of the bead-like nanoarchitectures samples is 251 $mAh \cdot g^{-1}$. After 6 cycles, the nanoarchitectures sample exhibits a reversible capacity as high as 146.0 $mAh \cdot g^{-1}$. After 50 cycles under the current density of 100 $mA \cdot g^{-1}$, the bead-like nanostructure samples remains 127 $mAh \cdot g^{-1}$, and its capacity fading per cycle from 6th to 50th is 0.26%. Fig. S6 displays the charge/discharge profiles under different cycles of β-300 sample at current density of 100 mA g^{-1}. As comparison, the initial capacity of β-NWs sample is 184 $mAh \cdot g^{-1}$, yielding a reversible capacity 99.4 $mAh \cdot g^{-1}$ after 6 cycles. Its capacity decreases to 75 $mAh \cdot g^{-1}$ after 50 cycles under the current density of 100 $mA \cdot g^{-1}$, and its capacity fading per cycle from 6th to 50th is 0.55%. Han and co-workers[15] reported the moundlily like β-$AgVO_3$ nanowires show the capacity of about 95 $mAh \cdot g^{-1}$ under the current density of 100 $mA \cdot g^{-1}$ after 50 times cycling. Liang et al.[30] reported the Ag/β-$AgVO_3$ hybrid nanorods have the capacity of about 106 $mAh \cdot g^{-1}$ under the current density of 100 $mA \cdot g^{-1}$ after 30 times cycling. Liang et al.[46] reported that the $AgVO_3$/graphene composite aerogels have the capacity of about 118.9 $mAh \cdot g^{-1}$ under the current density of 100 $mA \cdot g^{-1}$ after 50 times cycling. Other related literatures of reported β-$AgVO_3$ electrochemical performance are listed in Tab. S2. In means that when tested under the current density

of 100 $mA \cdot g^{-1}$, the capacity of our nanoarchitectures sample (127 $mAh \cdot g^{-1}$) is higher than that of the samples previously reported. The enhanced discharge capacity of nanoarchitectures can be attributed to the bead-like nanostructure constructed from nanoparticles. Such nanoarchitectures possesses the higher specific surface area of 83 m^2 g^{-1} comparing with that of β-$AgVO_3$ nanowires sample (24 m^2 g^{-1})(Fig. S4), leads to the more effective contact areas of active materials and shorter lithium ion diffusion paths, which helps to improve the discharge capacity and cycling performance.[47] In addition, at the current densities range from 20 to 500 $mA \cdot g^{-1}$, the bead-like nanostructure still displays the better discharge capacity than that of the β-NWs sample (Fig. S7a). The Cyclic voltammograms (CVs) and first charge/discharge profiles at various current densities of the electrodes were shown in Fig. S7b.

The EIS measurements were conducted on the half-cells after the cyclability measurements. As shown in Fig. 10b, the EIS Nyquist plots of the bead-like β-300 nanostructure samples and the β-NWs sample have similar shape, composing of a depressed semicircle in the high-frequency region and an oblique line with an angle of 45° relative to the real axis in the low-frequency region. The semicircle reflects the charge-transfer impedance at the solid/electrolyte interface. The oblique line at low frequencies, designating to Warburg impedance, refers to the diffusion limitations for lithium ion insides the $AgVO_3$. A smaller diameter of the semicircle represents smaller charge transfer impedance.[48] It can be seen that the charge transfer resistance of the bead-like nanostructure is lower than that of the β-NWs, because of the higher contact area between active material and electrolyte. The overall length of the Warburg line is indicative of Li^+ ion diffusion limitations in the material.[48] The bead-like nanostructure presents a shorter Warburg region than that of the β-NWs sample, which is expected due to the smaller nanoparticle size resulting markedly smaller diffusion lengths in the former. The electrochemical performance of β-200 sample is shown in Fig. S8, and is discussed in Supporting

Information.

The significantly improved electrochemical properties of the 1D bead-like β-$AgVO_3$ nanoarchitectures electrodes may result from the following two factors. One is the fast kinetics related to the unique 1D bead-like nanoarchitecture materials. The interfaces of the nanoparticles are much closer than the corresponding single crystal particle, leading to a higher Li^+ diffusion rate and faster electronic kinetics.[49, 50] The other factor is the relatively high specific surface areas of bead-like nanoarchitectures, which provides more active sites for the contact between active material and electrolyte, decreases the polarization of the electrode,[35] and allows the rapid electrolyte transport.[51, 52]

Conclusions

The 1D bead-like $AgVO_3$ nanoarchitectures were successfully obtained by soft chemical *in-site* synthesis process using 2D plate like $K_2V_6O_{16}\cdot 2.7H_2O$ as precursor under the room temperature condition. In the $AgNO_3$ solution, the $AgVO_3$ nanocrystals were overgrown on the $K_2V_6O_{16}\cdot 2.7H_2O$ surface, forming the 2D platelike $K_2V_6O_{16}/AgVO_3$ composites. As the reaction time prolongs, 2D platelike composites transformed into the 1D $K_2V_6O_{16}/AgVO_3$ composites. At last, the residual $K_2V_6O_{16}$ within the 1D composite generally expended to generate $AgVO_3$ nanocrystals through *in site* crystallization process, forming 1D bead-like $AgVO_3$ nanostructures. The unique 1D bead-like β-$AgVO_3$ nanostructures possess the higher initial capacity of 251 $mAh\cdot g^{-1}$. After 50 cycles under the current density of 100 $mA\cdot g^{-1}$, the 1D bead-like nanoarchitectures cathode still has a higher discharge capacity (127 $mAh\cdot g^{-1}$) than that of 1D nanowires (75 $mAh\cdot g^{-1}$), mainly due to the larger specific surface area and fine particles constructed architectures. Therefore, it is believed that the soft chemical synthesis is an efficient method for designing and preparing the functional nanoarchitectures.

Supporting Information

TG-DTA curves of the α-$AgVO_3$ product, XPS spectrum of the β-$AgVO_3$ sample, TEM and HRTEM images of β-$AgVO_3$ nanowires, nitrogen adsorption/desorption isotherms of products, additional TEM images of the $K_2V_6O_{16}\cdot 2.7H_2O$/α-$AgVO_3$ composite, temporal evolution pH value of the system, part of electrochemical performances data. This material is available free of charge via the Internet at http://pubs.rsc.org.

Corresponding author

School of Materials Science and Engineering, Shaanxi University of Science and Technology, Weiyang, Xi'an, Shaanxi 710021, PR China

*E-mail: huangjf@sust.edu.cn, davidemt@126.com

Acknowledgments

The authors acknowledgment the support of Project Supported by the research starting foundation from Shaanxi University of Science and Technology(BJ12-22), Innovation Team Assistance Foundation of Shaanxi University of Science & Technology (Program No. TD12-05), Innovation Team Assistance Foundation of Shaanxi Province (Program No. 2013KCT-06), and the Natural Science Foundation of China (NO. 21173003).

References

(1) Q. Feng, M. Hirasawa and K. Yanagisawa, *Chem. Mater*., 2001, **13**, 290.

(2) P. Wen, H. Itoh, W. Tang and Q. Feng, *Langmuir*, 2007, **23**, 11782.

(3) C. Antonyraj, D. Srivastava, G. Mane, S. Sankaranarayanan, A. Vinu and K. Srinivasan, *J. Mater. Chem. A*, 2014, **2**, 6301.

(4) S. Paek, J. Kang, H. Jung, S. Hwang and J. Choy, *Chem. Commun.*, 2009, 7536.

(5) D. Hu, W. Zhang, Y. Tanaka, N. Kusunose, Y. Peng and Q. Feng, *Cryst. Growth Des.*, 2015, **15**, 1214.

(6) T. Ozawa, K. Fukuda, Y. Ebina and T. Sasaki, *Inorg. Chem.*, 2012, **52**, 415.

(7) X. Kong, D. Hu, Y. Ishikawa, Y. Tanaka and Q. Feng, *Chem. Mater.*, 2011, **23**, 3978.

(8) X. Kong, Y. Ishikawa, K. Shinagawa and Q. Feng, *J. Am. Ceram. Soc.*, 2011, **94**, 3716.

(9) L. Cao, Z. Guo, J. Huang, C. Li, J. Fei, Q. Feng, P. Wen, Y. Sun and X. Kong, *Mater. Lett.*, 2014, **137**, 110.

(10) X. Kong, Z. Guo, P. Wen, L. Cao, J. Huang, C. Li, J. Fei, F. Wang and Q. Feng, *RSC Adv.*, 2014, **4**, 56637.

(11) X. Kong, D. Hu, P. Wen, T. Ishii, Y. Tanaka and Q. Feng, *Dalton Trans.*, 2013, **42**, 7699.

(12) Y. Ding, Y. Wen, P. Aken, J. Maier and Y. Yu, *Chem. Mater.*, 2015, **27**, 3143.

(13) D. Yoon, K. Chung, W. Chang, S. Kim, M. Lee, Z. Lee and J. Kim, *Chem. Mater.*, 2015, **27**, 266.

(14) H. Park, T. Kim, J. Huh, M. Kang, J. Lee and H. Yoon, *ACS Nano,* 2012, **6**, 7624.

(15) C. Han, Y. Pi, Q. An, L. Mai, J. Xie, X. Xu, L. Xu, Y. Zhao, C. Niu, A. Khan and X. He, *Nano Lett.,* **2012**, ***12***, 4668.

(16) S. Zhang, J. Li, X. Wang, Y. Huang, M. Zeng, J. Xu, *J. Mater. Chem. A*, 2015, **3**, 10119.

(17) W. Zhao, J. Li, Z, Wei, S. Wang, H. He, C. Sun, S. Yang, *Appl. Catal., B*, 2015, **179**, 9.

(18) Z. Chen, S. Gao, R. Li, M. Wei, K. Wei and H. Zhou, *Electrochim. Acta*, 2008, **53**, 8134.

(19) E. Sorensen, H. Izumi, J. Vaughey, C. Stern and K. Poeppelmeier, *J. Am. Chem. Soc.*, 2005, **127**, 6347.

(20) Y. Xu, X. Han, L. Zheng, W. Yan and Y. Xie, *J. Mater. Chem.*, 2011, **21**, 14466.

(21) M. Whittingham, *Chem. Rev.*, 2004, **104**, 4271.

(22) S. Liang, J. Zhou, A. Pan, Y. Li, T. Chen, Z, Tian and H. Ding, *Mater. Lett.*, 2012, **74**, 176.

(23) H. Zeng, Q. Wang and Y. Rao, *RSC Adv.***,** 2015, **5**, 3011.

(24) S. Bao, Q. Bao, C. Li, T. Chen, C. Sun, Z. Dong, Y. Gan and J. Zhang, *Small*, 2007, **3**, 1174.

(25) L. Mai, L. Xu, Q. Gao, C. Han, B. Hu and Y. Pi, *Nano Lett.*, 2010, **10**, 2604.

(26) J. Song, Y. Lin, H. Yao, F. Fan, X. Li and S. Yu, *ACS Nano*, 2009, **3**, 653.

(27) J. Xie, X. Cao, J. Li, H. Zhan, Y. Xia and Y. Zhou, *Ultrason. Sonochem.*, 2005, **12**, 289.

(28) S. Liang, J. Zhou, X. Zhang, Y. Tang, G. Fang, T. Chen and X. Tan, *CrystEngComm*, 2013, **15**, 9869.

(29) Q. Wan, Y. Liu, Z. Wang, W. Wei, B. Li, J. Zou and N. Yang, *Electrochem. Commun.*, 2013, **29**, 29.

(30) S. Liang, J. Zhou, A. Pan, X. Zhang, Y. Tang, X. Tan and R. Wu, *J. Power Sources*, 2013, **228**, 178.

(31) Y. Wu, P. Zhu, X. Zhao, M. Reddy, S. Peng, B. Chowdari and S. Ramakrishna, *J. Mater. Chem. A*, 2013, **1** ,852.

(32) J. Xu, C. Hu, Y. Xi, B. Wan, C. Zhang and Y. Zhang, *Solid State Sci.*, 2012, **14**, 535.

(33) S. Kittaka, K. Matsuno and H. Akashi, *J. Solid State Chem.*, 1999, **142**, 360.

(34) X. Kong, Z. Guo, P. Wen, J. Huang, L. Cao, L. Yin, J. Li and Q. Feng, *CrystEngComm*, 2015, **17**, 3777.

(35) S. Zhang, W. Li, C. Li and J. Chen, *J. Phys. Chem. B*, 2006, **110**, 24855.

(36) Q. Feng, Y. Ishikawa, Y. Makita and Yamamoto, Y. *J. Ceram. Soc. Jpn.*, 2010, **118**, 141.

(37) R. Abe, M. Hara, J. Kondo, K. Domen, K. Shinohara and A. Tanaka, *Chem. Mater.*, 1998, **10**, 1647.

(38) H. Izawa, S. Kikkawa and M. Koizumi, *J. Phys. Chem.*, 1982, **86**, 5023.

(39) W. Zhao, Y. Guo, Y. Faiz, W. Yuan, C. Sun, S. Wang and S. Yang, *Appl. Catal., B*, 2015, **163**, 288.

(40) D. Murphy, P. Christian, F. DiSalvo and J. Waszczak, *Inorg. Chem.*, 1979, **18**, 2800.

(41) D. Singh, K. Polychronopoulou, C. Rebholz and S. Aouadi, *Nanotechnology*, 2010, **21**, 325601.

(42) Q. Bao, S. Bao, C. Li, X. Qi, C. Pan, J. Zang, W. Wang and D. Tang, *Chem. Mater*., 2007, **19**, 5965.

(43) A. Fairbrother, V. Izquierdo-Roca, X. Fontané, M. Ibáñez, A. Cabot, E. Saucedo and A. Pérez-Rodríguez, *CrystEngComm*, 2014, **16**, 4120.

(44) Y. Yu, S. Nam, O. Byungsung, K. Lee, Y. Choi, M. Yoon, P. Yu, *Mater. Chem. Phys.*, 2003, **78**, 149.

(45) S. Baskoutas and A. Terzis, *J. Appl. Phys.*, 2006, **99**, 013708.

(46) L. Liang, Y. Xu, Y. Lei and H. Liu, *Nanoscale*, 2014, **6**, 3536.

(47) E. Pohjalainen, T. Rauhala, M. Valkeapaa, J. Kallioinen and T. Kallio, *J. Phys. Chem. C*, 2015, **119**, 2277.

(48) Z. Xu, H. Wang, Z. Li, A. Kohandehghan, J. Ding, J. Chen, K. Cui and D. Mitlin, *J. Phys. Chem. C*, 2014, **118**, 18387.

(49) F. Cheng, J. Chen, X. Gou and P. Shen, *Adv. Mater.*, 2005, **17**, 2753.

(50) T. Ogasawara, A. Débart, M. Holzapfel, P. Novák and P. Bruce, *J. Am. Chem. Soc.*, 2006, **128**, 1390.

(51) F. Cheng and J. Chen, *J. Mater. Chem.*, 2011, **21**, 9841.

(52) L. Liang, H. Liu and W. Yang, *Nanoscale*, 2013, **5**, 1026.

Figure captions

Fig. 1 XRD patterns of (a) layered $K_2V_6O_{16}\cdot 2.7H_2O$ precursor, (b) the α-$AgVO_3$ product obtained by the treatment of $K_2V_6O_{16}\cdot 2.7H_2O$ precursor in $AgNO_3$ water solution at room-temperature for 24h, the β-$AgVO_3$ samples obtained by the heat-treatment of α-$AgVO_3$ product at (c) 200 and (d) 300 ^oC for 12 h, respectively.

Fig. 2 FE-SEM images of (a) layered $K_2V_6O_{16}\cdot 2.7H_2O$ precursor, (b) the α-$AgVO_3$ product obtained by the treatment of $K_2V_6O_{16}\cdot 2.7H_2O$ precursor in $AgNO_3$ water solution at room-temperature for 24h, the β-$AgVO_3$ samples obtained by the heat-treatment of α-$AgVO_3$ product at (c) 200 and (d) 300 ^oC for 2h, respectively.

Fig. 3 TEM images and HRTEM images of (a, b)the α-$AgVO_3$ product obtained by the treatment of $K_2V_6O_{16}\cdot 2.7H_2O$ precursor in $AgNO_3$ water solution at room-temperature for 24h, (c, d)the β-$AgVO_3$ samples obtained by the heat-treatment of α-$AgVO_3$ product at 300 ^oC.

Fig. 4 XPS spectra of the 1D bead-like α-$AgVO_3$ nanoarchitectures. (a) XPS survey spectrum of the sample, (b) XPS spectrum of the Ag 3d region, (c) XPS spectrum of the V 2p region.

Fig. 5 Raman spectra of (a)the 1D bead-like α-$AgVO_3$ nanoarchitectures, (b)β-200 sample, (c)β-300 sample and (d)the β-NWs sample , respectively.

Fig. 6 XRD patterns of the samples obtained by the treatment of $K_2V_6O_{16}·2.7H_2O$ precursor in $AgNO_3$ water solution at room-temperature for 0h, 1h, 4h, 6h, 8h, 12h, and 24h, respectively.

Fig. 7 FE-SEM images of the samples obtained by the treatment of $K_2V_6O_{16}·2.7H_2O$ precursor in $AgNO_3$ water solution at room-temperature for 1h, 4h, 8h, and 12h, respectively.

Fig. 8 TEM images and SAED patterns of the samples obtained by the treatment of $K_2V_6O_{16}·2.7H_2O$ precursor in $AgNO_3$ water solution at room-temperature for (a) 4h, (b) 8h, and (c) 12h, respectively.

Fig. 9 Formation mechanism of the 1D bead-like $AgVO_3$ nanoarchitectures from the layered $K_2V_6O_{16}·2.7H_2O$ platelike precursor.

Fig. 10 Cycling performance (a) of β-300 nanoarchitectures and β-$AgVO_3$ nanowires electrodes, tested at 100 mA g^{-1}, Nyquist plots (b) of β-300 nanoarchitectures and β-$AgVO_3$ nanowires electrodes, after 50 cycles.

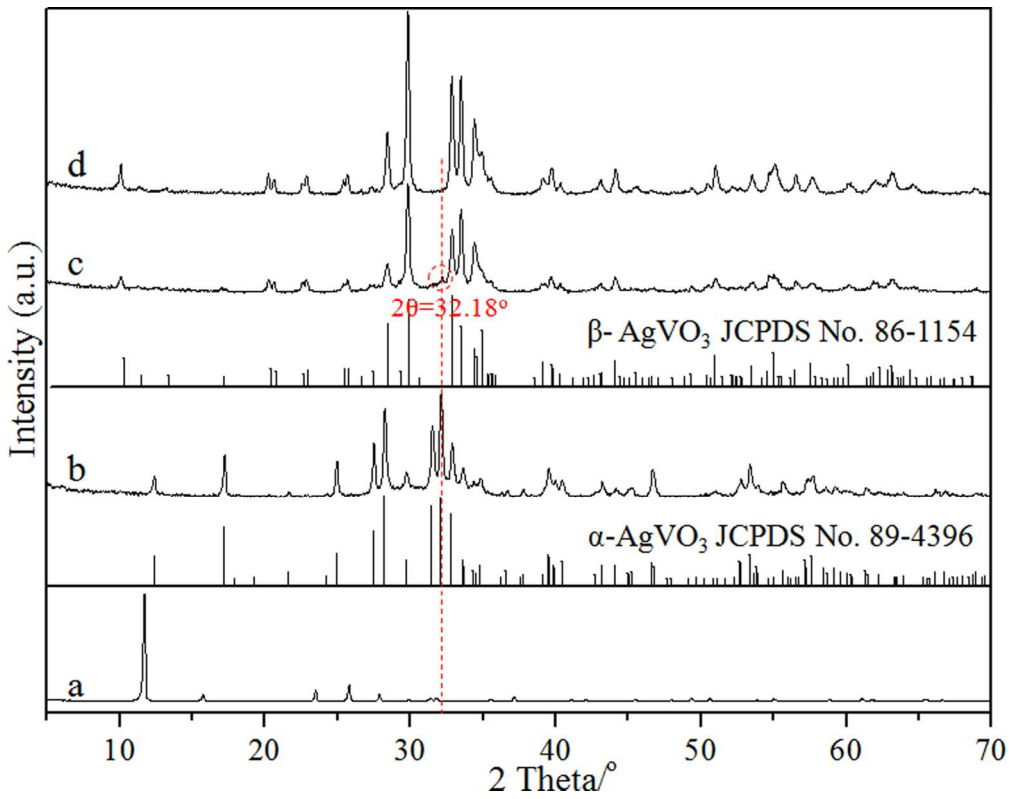

Fig. 1 XRD patterns of (a) layered K2V6O16·2.7H2O precursor, (b) the α-AgVO3 product obtained by the treatment of K2V6O16·2.7H2O precursor in AgNO3 water solution at room-temperature for 24h, the β-AgVO3 samples obtained by the heat-treatment of α-AgVO3 product at (c) 200 and (d) 300 oC for 12 h, respectively
62x49mm (600 x 600 DPI)

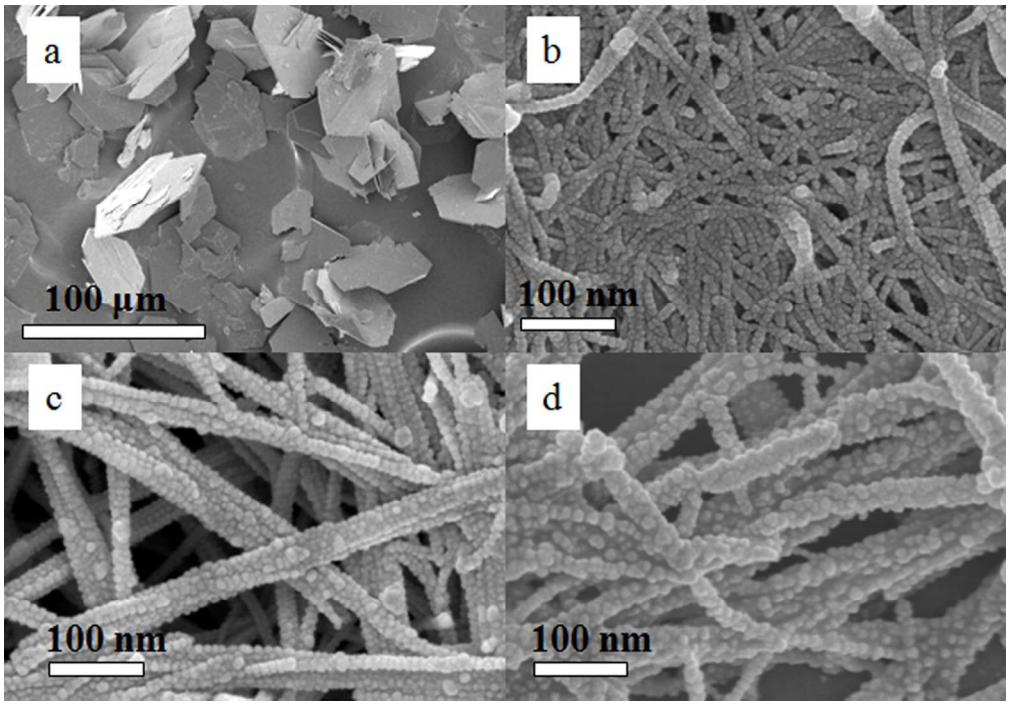

Fig. 2 FE-SEM images of (a) layered K2V6O16·2.7H2O precursor, (b) the α-AgVO3 product obtained by the treatment of K2V6O16·2.7H2O precursor in AgNO3 water solution at room-temperature for 24h, the β-AgVO3 samples obtained by the heat-treatment of α-AgVO3 product at (c) 200 and (d) 300 oC for 2h, respectively.
55x38mm (600 x 600 DPI)

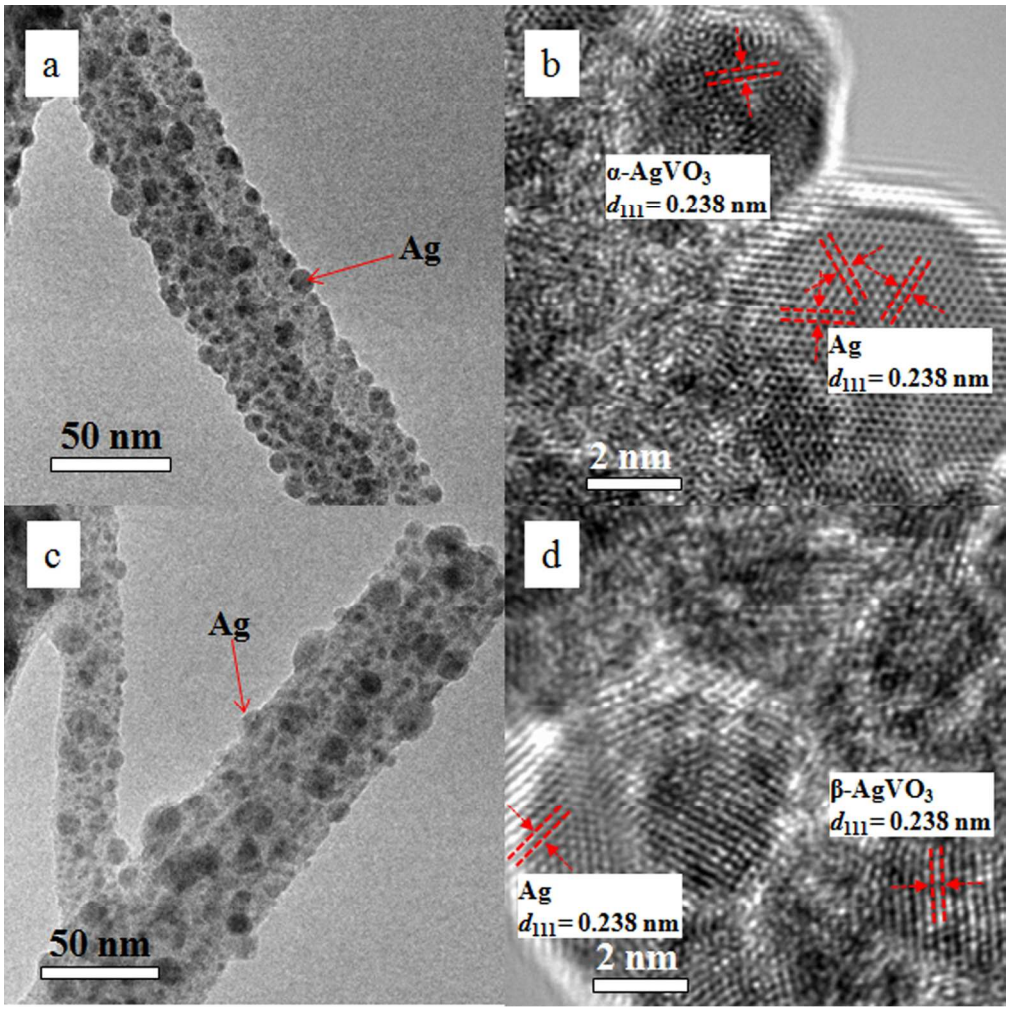

Fig. 3 TEM images and HRTEM images of (a, b)the α-AgVO3 product obtained by the treatment of K2V6O16·2.7H2O precursor in AgNO3 water solution at room-temperature for 24h, (c, d)the β-AgVO3 samples obtained by the heat-treatment of α-AgVO3 product at 300 oC.
80x80mm (600 x 600 DPI)

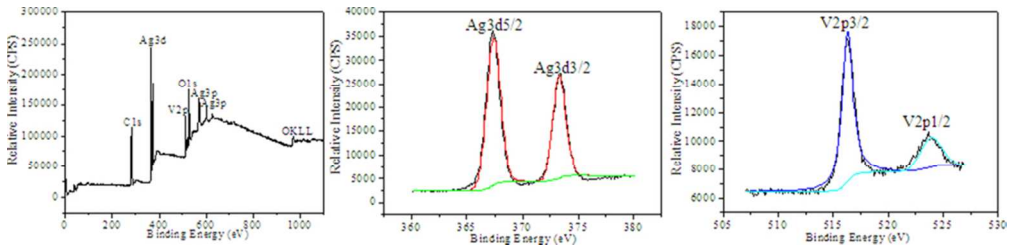

Fig. 4 XPS spectra of the 1D bead-like α-AgVO3 nanoarchitectures. (a) XPS survey spectrum of the sample, (b) XPS spectrum of the Ag 3d region, (c) XPS spectrum of the V 2p region.
37x9mm (600 x 600 DPI)

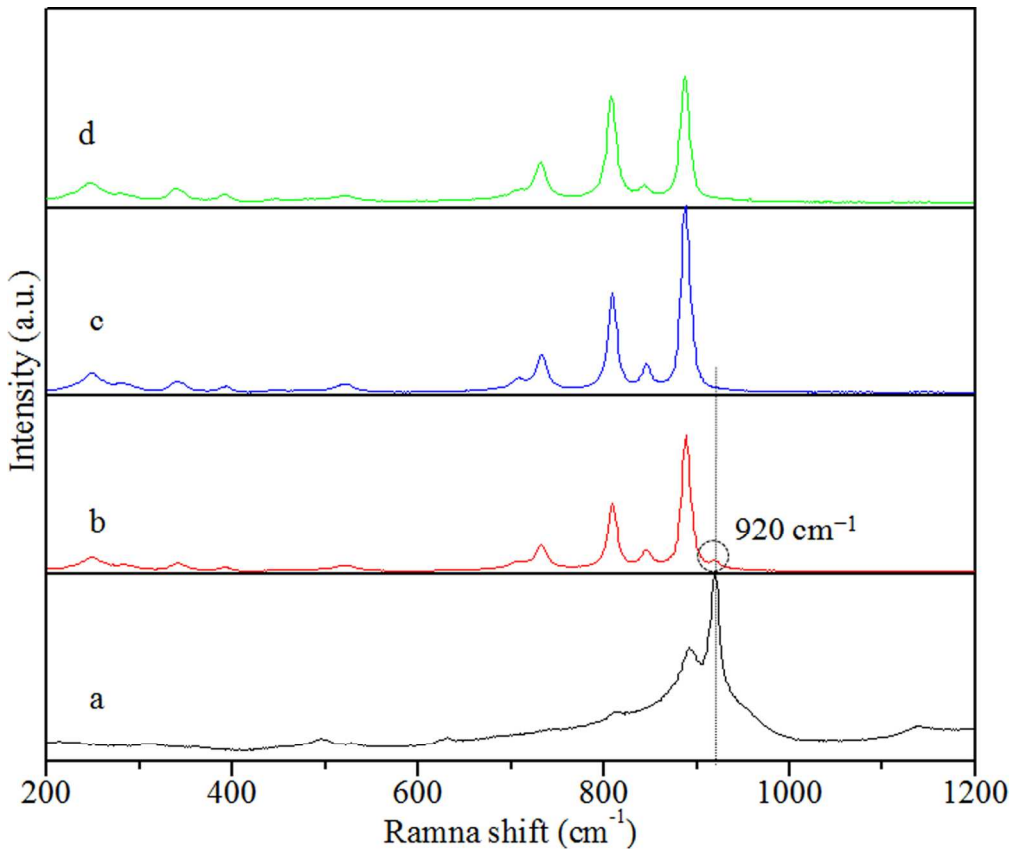

Fig. 5 Raman spectrum of (a)the 1D bead-like α-AgVO3 nanoarchitectures, (b)β-200 sample, (c)β-300 sample and (d)the β-NWs sample , respectively.
67x56mm (600 x 600 DPI)

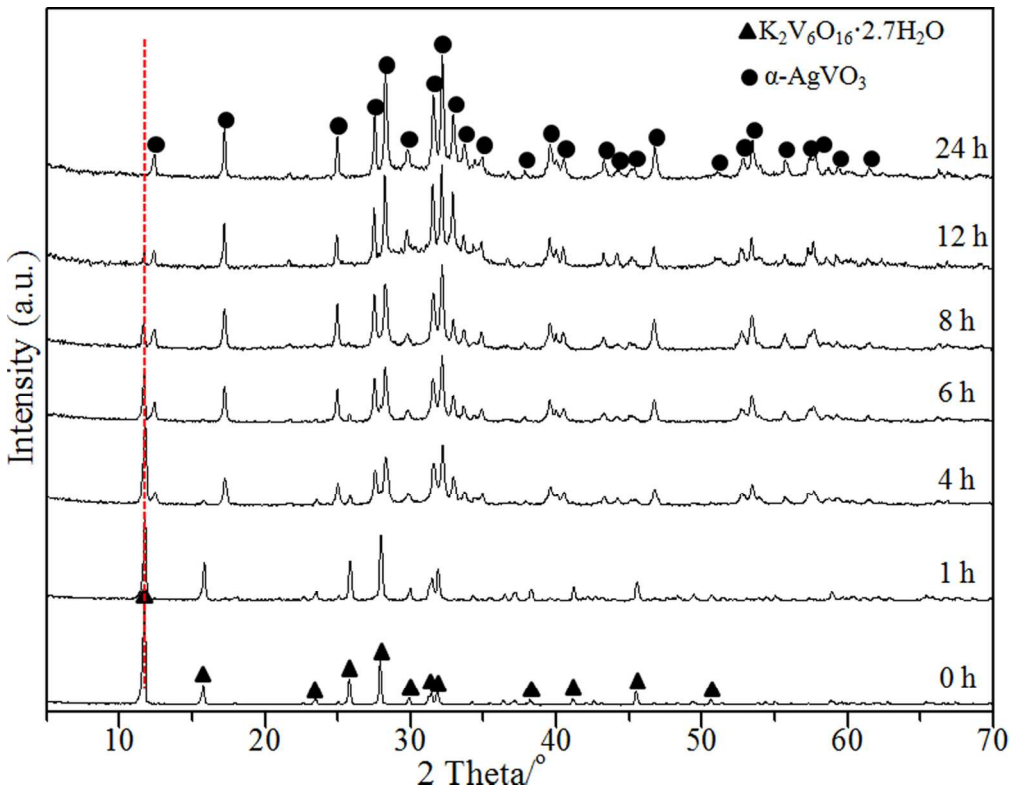

Fig. 6 XRD patterns of the samples obtained by the treatment of K2V6O16·2.7H2O precursor in AgNO3 water solution at room-temperature for 0h, 1h, 4h, 6h, 8h, 12h, and 24h, respectively.
62x48mm (600 x 600 DPI)

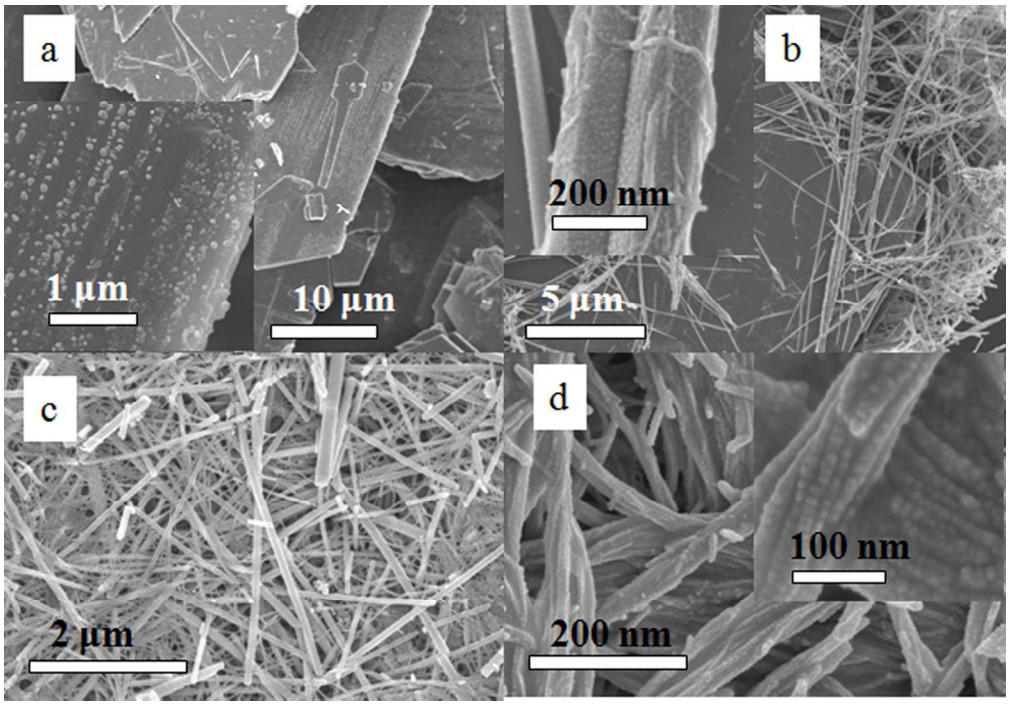

Fig. 7 FE-SEM images of the samples obtained by the treatment of K2V6O16·2.7H2O precursor in AgNO3 water solution at room-temperature for 1h, 4h, 8h, and 12h, respectively.
55x38mm (600 x 600 DPI)

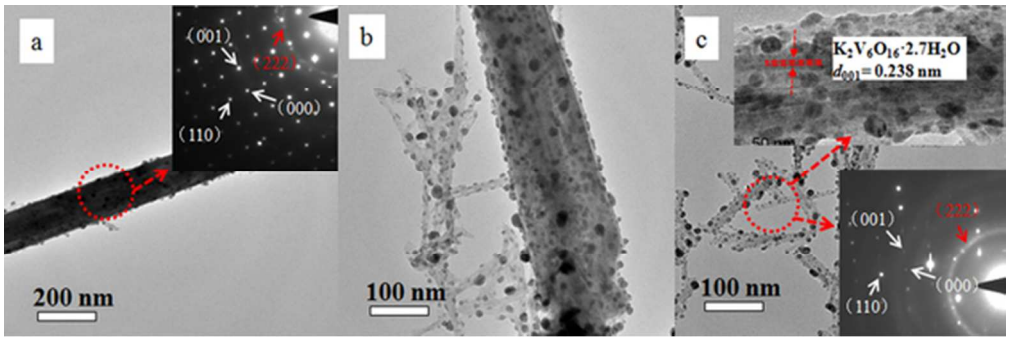

Fig. 8 TEM images and SAED patterns of the samples obtained by the treatment of K2V6O16·2.7H2O precursor in AgNO3 water solution at room-temperature for (a) 4h, (b) 8h, and (c) 12h, respectively.
26x8mm (600 x 600 DPI)

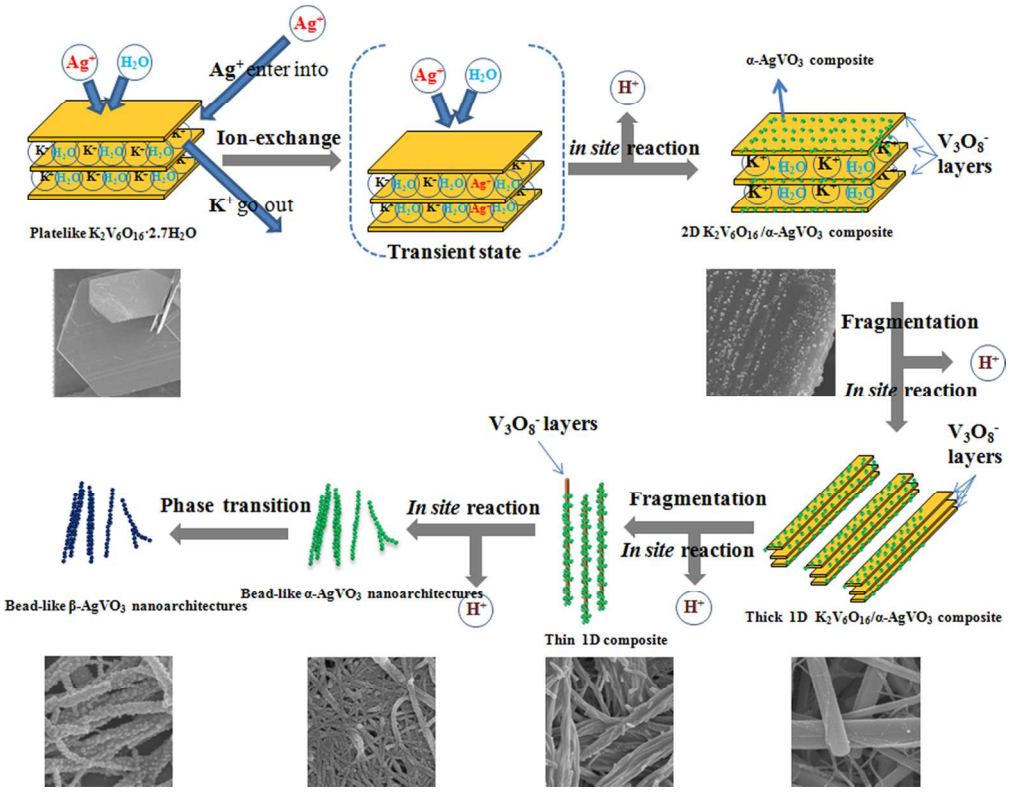

124x97mm (300 x 300 DPI)

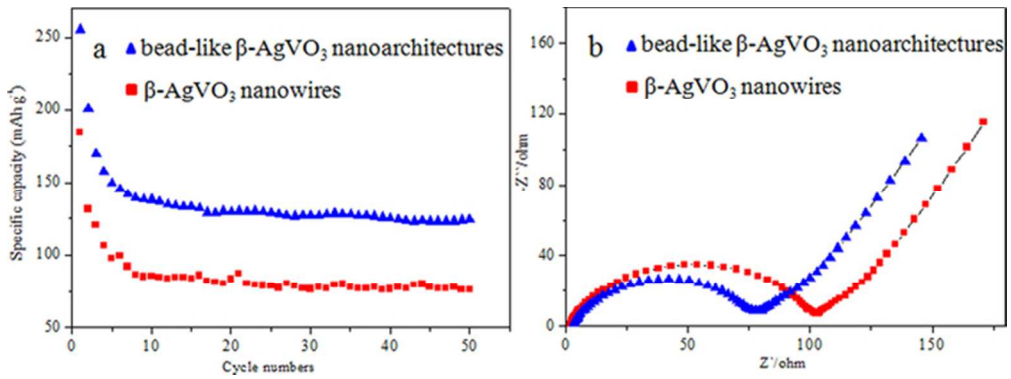

Fig. 10 Cycling performance (a) of β-300 nanoarchitectures and β-AgVO3 nanowires electrodes, tested at 100 mA g-1, Nyquist plots (b) of β-300 nanoarchitectures and β-AgVO3 nanowires electrodes, after 50 cycles.
29x10mm (600 x 600 DPI)

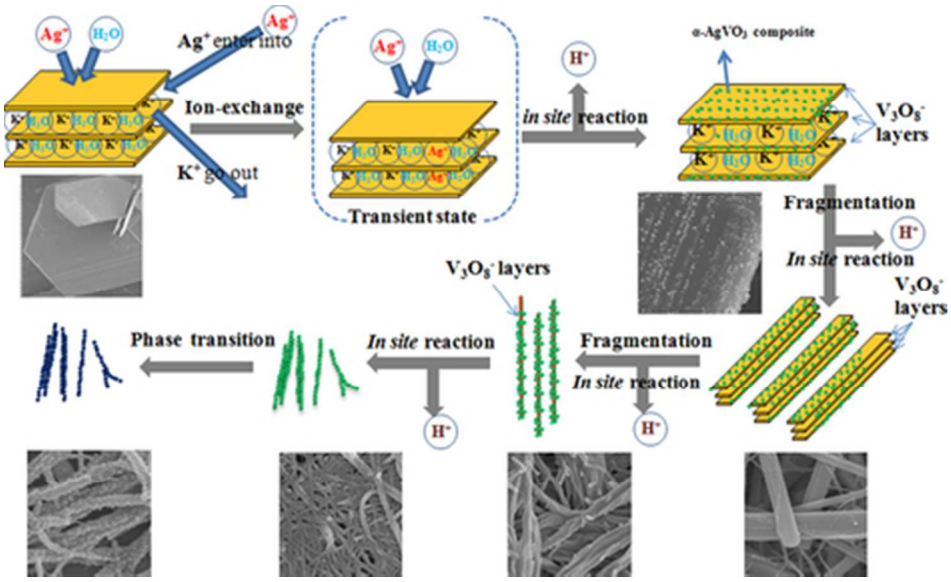

graphical abstracts
39x24mm (300 x 300 DPI)